

# Conceptual design of an experiment to study dust destruction by astrophysical shock waves

M. J.-E. Manuel<sup>1</sup>, T. Temim<sup>2</sup>, E. Dwek<sup>3</sup>, A. M. Angulo<sup>4</sup>, P. X. Belancourt<sup>4</sup>, R. P. Drake<sup>4</sup>, C. C. Kuranz<sup>4</sup>, M. J. MacDonald<sup>5</sup>, and B. A. Remington<sup>6</sup>

<sup>1</sup>General Atomics, 3550 General Atomics Court, San Diego, CA 92121, USA

<sup>2</sup>Space Telescope Science Institute, 3700 San Martin Drive, Baltimore, MD 21218, USA

<sup>3</sup>Observational Cosmology Lab, Code 665, NASA Goddard Space Flight Center, Greenbelt, MD 20771, USA

<sup>4</sup>Climate and Space Science and Engineering, University of Michigan, Ann Arbor, MI 48109, USA

<sup>5</sup>Department of Physics, University of California, Berkeley, CA 94720, USA

<sup>6</sup>Lawrence Livermore National Laboratory, Livermore, CA 94450, USA

(Received 20 November 2017; revised 16 March 2018; accepted 9 May 2018)

## Abstract

A novel laboratory experimental design is described that will investigate the processing of dust grains in astrophysical shocks. Dust is a ubiquitous ingredient in the interstellar medium (ISM) of galaxies; however, its evolutionary cycle is still poorly understood. Especially shrouded in mystery is the efficiency of grain destruction by astrophysical shocks generated by expanding supernova remnants. While the evolution of these remnants is fairly well understood, the grain destruction efficiency in these shocks is largely unknown. The experiments described herein will fill this knowledge gap by studying the dust destruction efficiencies for shock velocities in the range  $\sim 10\text{--}30$  km/s ( $\mu\text{m/ns}$ ), at which most of the grain destruction and processing in the ISM takes place. The experiments focus on the study of grain–grain collisions by accelerating *small* ( $\sim 1$   $\mu\text{m}$ ) dust particles into a *large* ( $\sim 5\text{--}10$   $\mu\text{m}$  diameter) population; this simulates the astrophysical system well in that the more numerous, *small* grains impact and collide with the *large* population. Facilities that combine the versatility of high-power optical lasers with the diagnostic capabilities of X-ray free-electron lasers, e.g., the Matter in Extreme Conditions instrument at the SLAC National Accelerator Laboratory, provide an ideal laboratory environment to create and diagnose dust destruction by astrophysically relevant shocks at the micron scale.

**Keywords:** laboratory astrophysics; shock waves; dust destruction

## 1. Introduction

Dust plays a crucial role in the evolution of the interstellar medium (ISM) through multiple physical processes, including the absorption, scattering and reradiation of starlight, the heating and cooling of gas, the facilitation of chemical reactions, the polarization of starlight and the depletion of heavy elements from the gas. It is an important diffuse foreground emission component that needs to be understood and removed in all studies of cosmological background radiations, such as the cosmic infrared background<sup>[1]</sup> and studies of the anisotropy and polarization of the cosmic microwave radiation<sup>[2]</sup>. Accurate knowledge of the dust-size distribution is required for proper modeling of dust contributions to the diffuse sky emission, and is therefore

crucial for deriving cosmological parameters from deep surveys of the universe.

Dust is formed in the violent ejecta of core collapse supernovae and in the quiescent winds of low-mass asymptotic giant branch stars and the more massive Wolf–Rayet stars<sup>[3]</sup>. Production rates of dust can be estimated from observations of resolved stellar populations in nearby galaxies such as the Magellanic Clouds (MCs)<sup>[4]</sup>. The dust destruction rates are, however, highly uncertain. Also available in the MCs is a complete inventory of all supernova remnants that are responsible for the current rate of dust destruction. It is believed that most of the dust is destroyed during the late evolution of the remnant, when it has slowed down to velocities  $< 100$  km/s. Kinetic sputtering, caused by the relative dust–gas motion, is then the dominant process of grain destruction. At velocities below  $\sim 30$  km/s the energy of the ions (predominantly hydrogen) falls below the sputtering threshold, and grain destruction by evaporation

Correspondence to: M. J.-E. Manuel, General Atomics, 3550 General Atomics Court, San Diego, CA 92121, USA.  
Email: [manuelm@fusion.gat.com](mailto:manuelm@fusion.gat.com)

and shattering in grain–grain (g–g) collisions becomes the dominant mechanism of dust destruction and processing. Most of the ISM volume is swept up during this phase of the remnant’s evolution. The outcome of these collisions, and the fraction of the dust mass that is evaporated or fragmented, however, are not well known. Previous estimates of the destruction efficiency are derived by scaling results from collisions between meter-sized rocks<sup>[5]</sup> because no experimental work at the proper scales has been performed.

Experiments described here will directly measure g–g destruction efficiencies of micron-sized dust particles in the  $\sim 5$ – $10\ \mu\text{m}$  range using a double dust-layer target based on previously successful experiments by Hansen *et al.*<sup>[6]</sup>. Accurately measuring micron-sized projectiles moving at speeds of  $\gtrsim 10\ \text{km/s}$  with micron resolution is achievable using the combination of capabilities from X-ray free-electron lasers (XFELs) and high-power drive beams. For the purposes of this design paper, present capabilities of the Matter in Extreme Conditions (MEC) instrument of the Linear Coherent Light Source (LCLS) will be used. However, other facilities with similar characteristics are under construction at SACLA in Japan and the High Energy Density instrument at the European XFEL in Germany.

These experiments aim to study astrophysical-shock processing of dust grains by measuring the evolution of *large* ( $\sim 5$ – $10\ \mu\text{m}$ ) dust grains as they are impacted by *small* ( $\lesssim 1\ \mu\text{m}$ ) dust grains. Measurements made in these experiments will improve our understanding of astrophysical dust evolution and will significantly impact future models of ISM dust and their diffuse emission. These results will provide the first experimental data to characterize dust destruction efficiencies of micron-sized dust grains in an astrophysically relevant regime.

## 2. Experimental setup

### 2.1. Target design

The experiments will use long-pulse optical beams to produce a shock wave that propagates through a low-density  $\text{SiO}_2$  foam containing the dust grains, as shown in Figure 1. Initial work will investigate the destruction of large diameter ( $\sim 5$ – $10\ \mu\text{m}$ ) dust grains through collisions with smaller grains ( $\lesssim 1\ \mu\text{m}$ ). The target consists of a Kapton washer with an inner diameter of  $500\ \mu\text{m}$  within which the foams are formed. The double-layer targets are built in a multi-step process where the foams containing the different size dust grains are created separately. The ‘nondusty’ side is covered with a  $\sim 13\ \mu\text{m}$  thick layer of Parylene C that will function as the ablator and the targets are finished with a flash-coating of  $1000\ \text{\AA}$  ( $1\ \text{\AA} = 0.1\ \text{nm}$ ) of aluminum, as shown in Figure 1(a).

We modeled the laser–target interaction for many dust and foam parameters using HYADES<sup>[7]</sup>, a 1D radiation

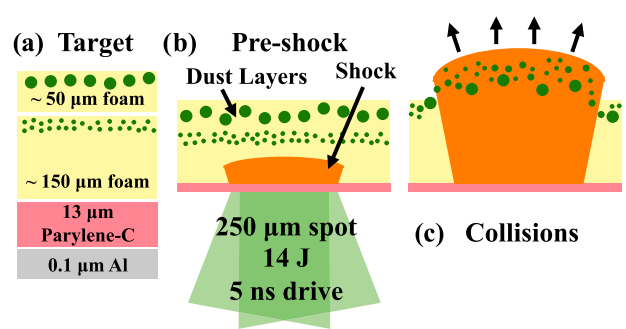


**Figure 1.** (a) Exploded view of the target layers. (b) Experimental schematic with drive parameters. Laser ablation drives a shock in the low-density foam. (c) When the shock passes the dust, *small* grains are accelerated to near the shock velocity and *large* grains to a fraction thereof, resulting in g–g collisions behind the shock.

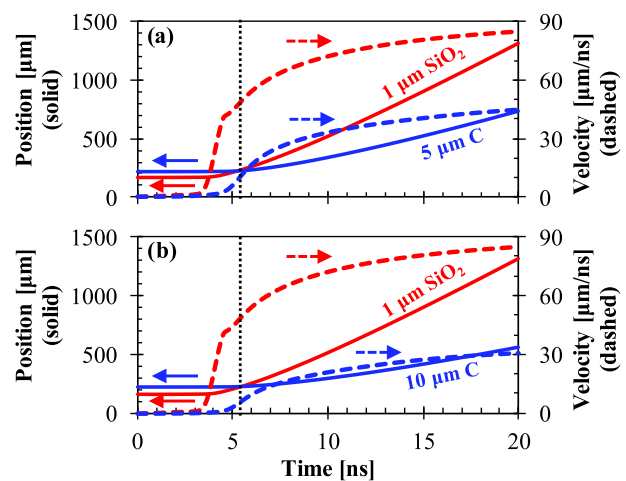


**Figure 2.** Summary of 1D HYADES results for a nominal case of *small* ( $1\ \mu\text{m}$  diameter)  $\text{SiO}_2$  grains impacting *large* carbon grains of (a)  $5\ \mu\text{m}$  and (b)  $10\ \mu\text{m}$  diameter. The mass-averaged position (solid) and velocity (dashed) are shown as a function of time. The vertical dotted line indicates the time ( $\gtrsim 5\ \text{ns}$ ) at which the *small* grains reach the *large* grains. The relative velocity between the grains in both cases is  $\sim 40\ \mu\text{m/ns}$ . These simulations used a  $25\ \text{mg/cc}$   $\text{SiO}_2$  foam.

hydrodynamic code. In the nominal configuration, a laser-driven shock is produced by ablating  $13\ \mu\text{m}$  of Parylene C with a  $5\ \text{ns}$  pulse containing  $14\ \text{J}$  of energy with an intensity of  $\sim 6 \times 10^{12}\ \text{W/cm}^2$ , assuming a  $250\ \mu\text{m}$  spot diameter. At this modest intensity, the  $13\ \mu\text{m}$  ablator is more than sufficient to prevent any burn-through, i.e., the laser does not deposit energy into the foam directly. Equation-of-state tables<sup>1</sup> were used for all materials, and zones at interfaces between different materials were mass-matched for accurate shock propagation between materials of different densities. In 1D, dust grains are modeled as a single layer of material with the expectation that the velocity is an overestimate due to the 3D nature of the real dust grain. Figure 2 summarizes

<sup>1</sup>Internal HYADES EOS/opacity tables were used: No. 35/1035 (Parylene), No. 41/1041 (aluminum), No. 22/1022 (quartz –  $\text{SiO}_2$ ) and No. 344/1344 (carbon).

the 1D results of the nominal case using the mass-averaged grain velocity and position as the metrics of interest.

These calculations indicate relative velocities between the *small* and *large* grain populations of  $\sim 38 \mu\text{m/ns}$  ( $5 \mu\text{m C}$ ) and  $\sim 42 \mu\text{m/ns}$  ( $10 \mu\text{m C}$ ). The foam density and *small* grain size provide experimental controls to alter the g–g collision velocity. These calculations are an overestimate of the true velocity because the shock will slip past the 3D dust grain – causing a drag force – and there will be momentum and energy transport in the transverse direction. From previous experience with these 1D codes, we expect the true velocities to be about half of the 1D values. This reduces the estimated relative velocity between *small* and *large* grains to  $\sim 20 \mu\text{m/ns}$ , still well within the  $10\text{--}30 \mu\text{m/ns}$  needed for relevance to astrophysical g–g collisions.

Our targets are designed to maximize shock uniformity. We expect much of the micron-scale speckle in the laser spot created by the phase plates to be annealed as the shock propagates through the  $13 \mu\text{m}$  ablator and  $\sim 150 \mu\text{m}$  of foam before reaching the *small* grains. The fine structure of the foam will create nonuniformities at the cell scale (a few  $100 \text{ nm}$ ), but these modulations will be much smaller in amplitude and, therefore, tolerable for the experimental goals. After passing through the *small* grains, the shock will have another  $\sim 50 \mu\text{m}$  to anneal before reaching the *large* grain population. The exact separation distance between the *small* and *large* grains should be at least  $50 \mu\text{m}$ , but the experimental design can handle up to  $\sim 100 \mu\text{m}$  separation without significantly changing the physics.

## 2.2. Grain–grain collisions

The primary focus of these experiments is to experimentally observe dust destruction of a *large* grain population due to g–g collisions with a *small* grain population. Grains are shock-accelerated to high speeds as discussed in the previous section. After passage of the shock, these grains exist within a plasma formed by the ionized foam. In general, they can be thought of as having an electric potential equal to that of the floating potential  $V_f \approx -T_e/(2e) \ln[m_i/(2\pi m_e)]$ , where  $m_i$  is the plasma-ion mass;  $T_e$ ,  $e$  and  $m_e$  are the electron temperature, charge and mass, respectively. For an  $\text{SiO}_2$  plasma at the few-eV level, the electric potential energy of these grains is  $\sim 10 \text{ s of eV}$ . At these thermal energies we also note that sputtering of either grain population due to the plasma ions is negligible. The kinetic energy of a  $1 \mu\text{m}$  diameter  $\text{SiO}_2$  dust grain moving at a relative speed of  $\sim 20 \mu\text{m/ns}$  is  $\sim 2.6 \times 10^{12} \text{ eV}$ . Due to the high kinetic energies involved and low plasma temperatures, g–g collisions are the dominant mechanism of dust destruction and can be simply thought of as occurring between ballistic projectiles where the number of collisions is set by the relative densities of the *small* and *large* grain populations.

**Table 1.** Sample target parameters for dust destruction experiments.

Target design	$E_{\text{BL}}/E_{\text{KS}}$	$N_L$	$m_L$ (ng)	$N_S$	$m_S$ (ng)	$\Delta_S$ ( $\mu\text{m}$ )
$1 \mu\text{m SiO}_2, 5 \mu\text{m C}$	$\sim 23$	300	45	$2.3 \times 10^5$	240	$\sim 1$
$1 \mu\text{m SiO}_2, 10 \mu\text{m C}$	$\sim 185$	300	360	$4.6 \times 10^5$	480	$\sim 2$

When designing these targets, the dust mass is used as the metric since it is weighed out prior to being added to the foam solution. The number of *large* dust grains ( $N_L$ ) is estimated by the target size, dust size and diagnostic technique; for the experiments described herein, we find that the number of  $\lesssim 300$  *large* grains is a good initial estimate. The number of *small* grains is determined by the required number of collisions to ‘destroy’ a *large* grain, which is estimated by setting the relative kinetic energy of the *small* grain ( $E_{\text{KS}}$ ) to the binding energy of the *large* grain ( $E_{\text{BL}}$ ). For example, the binding energy of vaporization per atom for graphite is  $\sim 8 \text{ eV}$ <sup>[8]</sup>. Hence, a  $5 \mu\text{m C}$  grain has  $\sim 60 \times 10^{12} \text{ eV}$  of binding energy. For a  $1 \mu\text{m SiO}_2$  grain carrying  $\sim 2.6 \times 10^{12} \text{ eV}$  of kinetic energy, complete *large* grain destruction requires  $\sim 23$  collisions. Since collisions are ballistic, this suggests that  $\gtrsim 23$  *small* grains are needed within the hydrodynamic column of a single *large* grain. For a target diameter  $D_{\text{targ}}$  and a *large* grain diameter  $D_L$ , the total number of *small* grains ( $N_S$ ) can be estimated by

$$N_S \approx \frac{D_{\text{targ}}^2 E_{\text{BL}}}{D_L^2 E_{\text{KS}}}. \quad (1)$$

The thickness of the *small* grain layer  $\Delta_S$  can be estimated after assuming a filling fraction<sup>2</sup>  $f_S \sim 2/3$  by

$$\Delta_S \approx D_S \frac{D_S^2 E_{\text{BL}}}{D_L^2 E_{\text{KS}}}. \quad (2)$$

Estimated values of these target parameters are listed in Table 1, for the two target configurations discussed in Figure 2. The values for  $\Delta_S$  suggest that the targets containing  $5 \mu\text{m C}$  grains require a near-monolayer of *small* dust grains, whereas the targets with  $10 \mu\text{m C}$  grains require essentially a double layer of  $1 \mu\text{m SiO}_2$  grains. Thin layers can be achieved by allowing the dust to settle in the foam solution prior to the solvent exchange process. These values are estimates and assume that all grains in the hydrodynamic column efficiently vaporize part of the *large* dust grain. In reality, each *small* grain will not be moving at exactly  $20 \mu\text{m/ns}$ , nor is the exact binding energy of every atom in the grain exactly  $8 \text{ eV}$ . However, this methodology provides the framework to estimate the dust mass necessary

<sup>2</sup>Defined as the ratio of the volume of grains to the occupied volume within the target and estimated as the ratio of the volume of a sphere,  $\frac{4}{3}\pi(\frac{D}{2})^3$ , to the volume of a cylinder,  $\pi(\frac{D}{2})^2 D$ .

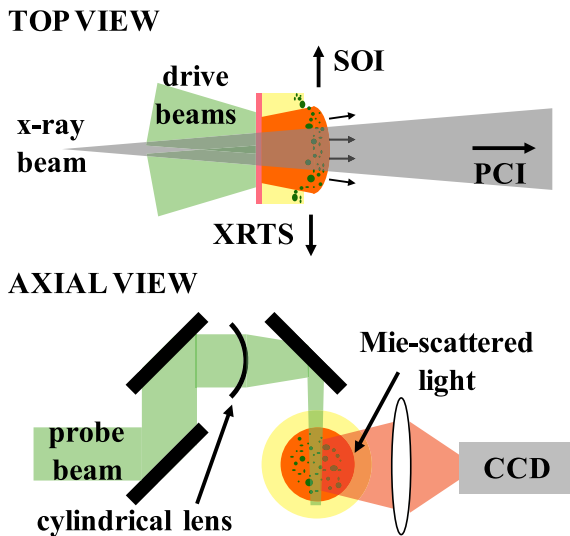


**Figure 3.** Top and axial views of the experimental geometry illustrating the targets and primary diagnostics.

to have a significant number of collisions for dust destruction experiments.

Grain–grain collisions are the dominant destruction mechanism of the *large* population. The shocked foam is expected to be at the few-eV level and, in theory, does not provide enough kinetic energy for a single ion to sputter away material from the dust grains. The lateral motion of the *large* grains can cause g–g collisions between grains in the *large* population, though the relative speed is substantially reduced since the bulk motion is axial. The bilayer design of these targets allows us to study the effect of this destruction mechanism by testing targets without the *small* grain population. In this way, dust destruction caused by collisions between *small* and *large* grains may be studied directly through experiments.

### 2.3. Experimental configuration

The primary physics goals of these experiments require measuring the size distribution of the *large* dust grains after the interaction with the *small* grain population. Figure 3 illustrates the experimental geometry for the incoming beams and diagnostic directions. Breakout of the shock from the rear surface of the target is measured using a streaked optical imager (SOI) that is timed with the drive beams. For present capabilities at MEC, the X-ray beam is run at 8.2 keV for phase-contrast imaging (PCI)<sup>[9]</sup> of the dust distribution and for measuring plasma conditions using an X-ray Thomson spectrometer (XRTS). The 1D velocity distribution of the dust grains is characterized using a separate optical probe beam and a cylindrical lens, as shown by the axial view of Figure 3. In this configuration, Mie-scattered light from the

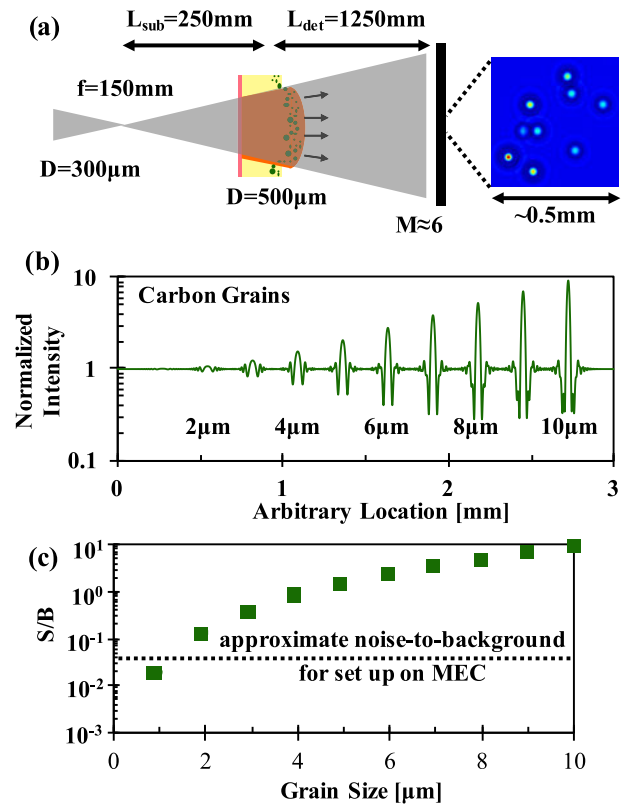


**Figure 4.** (a) Imaging geometry for the PCI diagnostic on MEC with an initial beam diameter  $D = 300 \mu\text{m}$ . A  $500 \mu\text{m}$  square area in the detector plane of a simulated 8.2 keV phase-contrast image. The simulation implemented randomly distributed 5–10  $\mu\text{m}$  C grains, a finite source size ( $\sim 100 \text{ nm}$ ) and instrumental broadening. (b) Simulated diffraction patterns in X-ray intensity from carbon grains for this PCI setup normalized to the background X-ray intensity. (c) The  $S/B$  value is the measured peak-to-valley intensity relative to the background intensity and is shown for the different carbon grain sizes in (b). Abbreviation:  $S/B$ , signal to background.

dust grains is measured on a gated camera using a particle imaging velocimetry technique<sup>[6]</sup>.

The size distribution of *large* dust grains is characterized by the PCI diagnostic utilizing the XFEL. Figure 4 illustrates the proposed PCI geometry using 8.2 keV X-rays. The beam is focused to a  $\sim 100 \text{ nm}$  – full width at half maximum (FWHM) – spot<sup>[9]</sup> using a series of  $\sim 30$  Be lenses for an effective focal length of 150 mm. Targets are placed 250 mm from the focal point so that the beam expands to the number of  $\sim 300 \mu\text{m}$  and the X-rays are detected on a Ce:YAG screen 1250 mm from the target. Optical emission from the screen is imaged onto a charge-coupled device (CCD) using a  $10\times$  microscope providing  $\sim 1 \mu\text{m}$  ( $\sim 170 \text{ nm}$ ) resolution with a  $\sim 3.7 \text{ mm}$  ( $\sim 620 \mu\text{m}$ ) field of view at the screen (target). The *large* dust population is imaged with 50 fs X-ray pulses, which is shorter than the evolutionary time scale of the system, and the shock is effectively stationary over the probe time.

We developed a simulator for the PCI diagnostic to examine the expected contrast levels in our experiments as

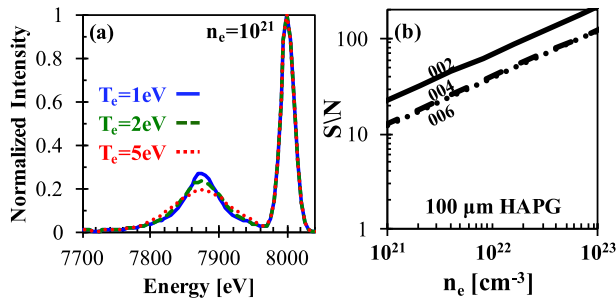


**Figure 5.** (a) Simulated Thomson spectra for the proposed geometry using an 8.2 keV beam with an FWHM of 20 eV and the plasma parameters indicated. (b) Photonics calculations, where  $S/N = \sqrt{N}$ , for the diffraction orders  $n = 2, 4$  and  $6$  using the 100  $\mu\text{m}$  HAPG crystal with an initial photon count of  $10^{12}$  and 10 eV energy bins at the detector. Abbreviation: HAPG, highly annealed pyrolytic graphite.

demonstrated by the sample image in Figure 4. A summary of the expected phase contrast in the proposed geometry is given in Figure 4 for carbon grains of various sizes. The proposed setup produces Fresnel numbers ( $N_F = a^2/\lambda z$ , with grain size  $a$ , photon wavelength  $\lambda$  and effective propagation distance  $z$ )  $< 1$ , indicating that our measurements are made in the Fraunhofer diffraction limit. This can be seen by the simulated image shown in Figure 4 of randomly distributed 5–10  $\mu\text{m}$  C grains over a 500  $\mu\text{m} \times 500 \mu\text{m}$  region. These dust grains create small diffraction patterns where the central intensity variation and diameter correspond to the grain size. However, intensity variation is the more sensitive measurement in this experiment and the one-to-one correspondence with grain size is illustrated in Figure 4(c) for carbon dust. Therefore the ‘signal’ we measure is the peak-to-valley amplitude of the primary peak and first minimum in the diffraction pattern. However, it is the background-normalized amplitude, or signal-to-background ( $S/B$ ) measurement, that we care about. We expect unwanted amplitude modulations in our image due to the *small* grains and X-ray beam nonuniformities of the order of  $S/B \approx 0.04$ . This represents our ‘noise-to-background’ floor as shown in Figure 4(c). Grain sizes  $\gtrsim 2 \mu\text{m}$  will be resolvable with  $\frac{\Delta a}{a} \approx \frac{3}{8} \frac{\Delta S/B}{S/B}$ , e.g., a measurement of  $S/B = 0.1 \pm 0.01$  indicates a grain size of  $1.83 \pm 0.07 \mu\text{m}$ . Grain-size distributions are measured directly from the diffraction patterns in PCI data, shock breakout is determined using the SOI diagnostic, and plasma conditions can be determined through XRTS by collecting scattered photons from the same beam used for PCI.

High-resolution XRTS spectra are taken perpendicular to the flow, as indicated in Figure 3, to spatially resolve the plasma expansion. A 100  $\mu\text{m}$  slit is aligned with the shock propagation direction to image the scattered spectrum and infer plasma properties of the shocked material and of the front itself. The same XFEL pulse used to image the grains is used for Thomson scattering and by changing the relative time between the drive pulse and X-ray beam, evolution

of both the dust-size distribution and the plasma properties may be studied. Thomson scattering will occur in the noncollective regime ( $\alpha < 1$ ) in the proposed geometry for the expected densities ( $\sim 10^{22} \text{ cm}^{-3}$ ) and temperatures ( $\sim 2$ –5 eV) of the  $\text{SiO}_2$  plasma created by the foam, producing the simulated spectra shown in Figure 5(a). The 100  $\mu\text{m}$  highly annealed pyrolytic graphite (HAPG) crystal is selected to provide increased reflectivity while still providing excellent energy resolution;  $E/\Delta E \sim 1000$  ( $\Delta E_{8.2 \text{ keV}} \sim 8 \text{ eV}$ ) for a 100  $\mu\text{m}$  slit at diffraction orders  $n = 2, 4$  and  $6$ <sup>[10]</sup>. The scattered X-rays are detected on a PI-MTE CCD. Photonics calculations<sup>[11]</sup> shown in Figure 5(b) indicate a high ( $> 10$ ) signal-to-noise ratio (SNR) for electron densities  $\gtrsim 10^{21} \text{ cm}^{-3}$  using the proposed geometry and detector with 4 mm Be shielding. Data will be averaged over multiple shots with the same timing to improve the SNR and determine plasma properties near the shock.

### 3. Summary

We have described experiments that will provide the first 2D images of shock-processed dust and experimentally measure destruction efficiencies of micron-sized grains under astrophysically relevant conditions. This work will provide valuable insight into an important, and unexplored phase of dust evolution in galaxies. By utilizing double dust-layer targets with *small* and *large* dust populations, we are focusing the investigation on g–g collisions and the resulting evaporation and fragmentation of dust particles at astrophysically relevant velocities of  $\sim 10$ –30  $\mu\text{m}/\text{ns}$ . Null experiments with only a *large* dust population will also directly demonstrate the destruction efficiencies of strong shocks on dust grains with sizes of  $\sim 5$ –10  $\mu\text{m}$  and self-consistently account for any ion sputtering that may occur due to the background plasma. As primary constituents of the ISM, carbon and silica particles are of the most interest and will be studied.

### 4. Experimental procedure

Prior to each driven shot, a PCI will be taken of the target to characterize the initial *large* grain population. The timing of each shot is controlled by the temporal separation between the drive beams and the X-ray pulse. This timing will vary to study the evolution of the grain-size distribution and to infer the g–g destruction efficiencies under those conditions. It is expected that the size distribution will shift to smaller diameters at later times due to fragmentation and evaporation caused by g–g collisions. Our PCI calculations indicate that the foam density has no measurable effect on the contrast image and that the *small* grain population only slightly increases the noise floor to a few percentage of the background. The short shot cycle achievable at the MEC

instrument at LCLS and other similar facilities provides the opportunity to study multiple grain materials under different shocked conditions with unprecedented diagnostic capabilities.

### Acknowledgements

Special thanks are given to David Montgomery for help in simulating X-ray phase-contrast images and Bob Nagler for in-depth discussions of the capabilities of the MEC instrument of the LCLS at the SLAC National Accelerator Laboratory. This work was funded by the US Department of Energy, through the NNSA-DS and SC-OFES Joint Program in High-Energy-Density Laboratory Plasmas, grant number DE-NA0001840. Additional support for this work was provided by NASA through Einstein Postdoctoral Fellowship grant number PF3-140111 awarded by the Chandra X-ray Center, which is operated by the Astrophysical Observatory for NASA under contract NAS8-03060.

### References

1. M. G. Hauser and E. Dwek, *Annu. Rev. Astron. Astrophys.* **39**, 249 (2001).
2. C. L. Bennett, D. Larson, J. L. Weiland, N. Jarosik, G. Hinshaw, N. Odegard, K. M. Smith, R. S. Hill, B. Gold, M. Halpern, E. Komatsu, M. R. Nolta, L. Page, D. N. Spergel, E. Wollack, J. Dunkley, A. Kogut, M. Limon, S. S. Meyer, G. S. Tucker, and E. L. Wright, *Astrophys. J. Suppl. Ser.* **208**, 20 (2013).
3. E. Dwek and I. Cherchneff, *Astrophys. J.* **727**, 63 (2011).
4. T. Temim, E. Dwek, K. Tchernyshyov, M. L. Boyer, M. Meixner, C. Gall, and J. Roman-Duval, *Astrophys. J.* **799**, 158 (2015).
5. K. J. Borkowski and E. Dwek, *Astrophys. J.* **454**, 254 (1995).
6. J. F. Hansen, W. van Breugel, E. M. Bringa, B. Eberly, G. A. Graham, B. A. Remington, E. A. Taylor, and A. G. G. M. Tielens, *J. Instrum.* **6**, P05010 (2011).
7. J. T. Larsen and S. M. Lane, *J. Quant. Spectrosc. Radiat. Transfer* **51**, 179 (1994).
8. L. Serra Diaz-Cano and A. P. Jones, *Astron. Astrophys.* **492**, 127 (2008).
9. B. Nagler, B. Arnold, G. Bouchard, R. F. Boyce, R. M. Boyce, A. Callen, M. Campell, R. Curiel, E. Galtier, J. Garofoli, E. Granados, J. Hastings, G. Hays, P. Heimann, R. W. Lee, D. Milathianaki, L. Plummer, A. Schropp, A. Wallace, M. Welch, W. White, Z. Xing, J. Yin, J. Young, U. Zastra, and H. J. Lee, *J. Synchrotron Radiat.* **22**, 520 (2015).
10. U. Zastra, A. Woldegeorgis, E. Förster, R. Loetzsch, H. Marschner, and I. Uschmann, *J. Instrum.* **8**, P10006 (2013).
11. S. H. Glenzer and R. Redmer, *Rev. Mod. Phys.* **81**, 1625 (2009).